frontiers | Frontiers in Materials

TYPE Original Research
PUBLISHED 30 May 2023
DOI 10.3389/fmats.2023.1214543

OPEN ACCESS

EDITED BY
Hairong Xue,
National Institute for Materials Science, Japan

REVIEWED BY
Huabin Zhang,
King Abdullah University of Science and Technology, Saudi Arabia
Lifeng Chen,
University of Science and Technology of China, China
Liang Wang,
Zhejiang University of Technology, China

*CORRESPONDENCE
Yongle Li,
yongleli@shu.edu.cn
Junfeng Rong,
rongjf.ripp@sinopec.com
Xuebin Wang,
wangxb@nju.edu.cn

†These authors have contributed equally to this work and share first authorship

RECEIVED 03 May 2023
ACCEPTED 15 May 2023
PUBLISHED 30 May 2023

CITATION
Wang T, Zeng J, Gu X, Meng Y, Yang H, Zhu H, Deng D, Sun Z, Ding R, Li Y, Rong J and Wang X (2023), *In-situ* growth of nitrogen-doped carbon nanotubes on MXene nanosheets for efficient sodium/potassium-ion storage.
Front. Mater. 10:1214543.
doi: 10.3389/fmats.2023.1214543

In-situ growth of nitrogen-doped carbon nanotubes on MXene nanosheets for efficient sodium/potassium-ion storage

Tao Wang[1†], Jinjue Zeng[1†], Xianrui Gu[2†], Yuhang Meng[1], Han Yang[1], Hongda Zhu[1], Dingfei Deng[1], Zhipeng Sun[1], Rui Ding[1], Yongle Li[3]*, Junfeng Rong[2]* and Xuebin Wang[1]*

[1]National Laboratory of Solid State Microstructures (NLSSM), Collaborative Innovation Center of Advanced Microstructures, Jiangsu Key Laboratory of Artificial Functional Materials, College of Engineering and Applied Sciences, Nanjing University, Nanjing, China, [2]Research Institute of Petroleum Processing, Beijing, China, [3]Department of Physics, International Center for Quantum and Molecular Structures, and Shanghai Key Laboratory of High Temperature Superconductors, Shanghai University, Shanghai, China

For game changing for future of large-scale energy storage technologies, sodium-ion and potassium-ion batteries provide a substitute to lithium-ion batteries. As an excellent candidate anode, MXene still suffers from the blockage of active sites caused by restacking of sheets. Herein, an *in-situ* decoration of MXene nanosheets with nitrogen-doped carbon nanotubes (CNTs) is introduced, to yield MXene@CNTs. The modification of nitrogen-doped CNTs not only prevents the restacking of MXene and increases ion accessibility but also improves the electrode's overall conductivity, thereby enhancing electron conduction and ion diffusion kinetics significantly. Therefore, MXene@CNTs exhibits superior sodium/potassium-ion storage performance than pure MXene nanosheets. At 0.05 A g^{-1}, it can deliver reversible capacities of 286 mAh g^{-1} for SIBs and 250 mAh g^{-1} for PIBs. This research illustrates the significance of the electrode architecture for electrochemical performances, and the *in-situ* growth strategy could provide some insight on searching for high-performance MXene-based anodes for SIBs and PIBs.

KEYWORDS

MXene, carbon nanotube, anode, sodium-ion batteries, potassium-ion batteries

1 Introduction

The global energy landscape is undergoing a significant transformation, propelled by the expansion of electric cars and the incorporation of clean energy systems (Luo et al., 2015; Zhang et al., 2020; Tian et al., 2021; Zhu et al., 2022; Huang et al., 2023). It is anticipated that battery technologies will play crucial roles in meeting this demand, helping to alleviate the range anxiety of electric vehicles and the intermittency of renewable energy sources (Dunn et al., 2011; Luo et al., 2015). Due to their high energy density, lithium-ion batteries (LIBs), which were commercialized in 1991, have enjoyed tremendous success in numerous sectors (Armand and Tarascon, 2008; Chou and Yu, 2017). However, energy storage battery demand will soar from 340 GWh in 2021–5,600 GWh in 2030 under the Net Zero Emissions Scenario (IEA, 2022). The scarcity of lithium and its unequal regional distribution have sparked interest in alternative battery technologies (Lin et al., 2015; Sun et al., 2015; Li et al., 2022).

Given their abundant resources, low cost, environmental friendliness, and good electrochemical performance, sodium-ion batteries (SIBs) and potassium-ion batteries (PIBs) are viewed as two ideal alternatives (Yabuuchi et al., 2014; Hosaka et al., 2020; Shi et al., 2021). Efficient electrode materials are very important for the widespread use of SIBs and PIBs, especially anodes.

MXene is a family of two-dimensional nanomaterials with desirable properties for use as electrodes, including high metallic conductivity and good chemical stability (Ghidiu et al., 2014; Naguib et al., 2014; Wang et al., 2018). For instance, theoretical calculation proves that the capacities for sodium-ion and potassium-ion on $Ti_3C_2M_x$ are 352 and 192 mAh g^{-1}, respectively. Their unique two-dimensional (2D) morphology and suitable interlayer spacing are conducive to lowering the ion diffusion barrier and increasing the number of ion adsorption sites (Lukatskaya et al., 2013; Liang et al., 2015; Yang et al., 2015; Zhao et al., 2015; Wu et al., 2021). Thus, they are possible to deliver high capacity and high-rate storage of metal ions. Nevertheless, MXene is still plagued by restacking and ion inaccessibility problems, which result in relatively low capacity, rapid performance degradation, and large volume expansion in SIBs and PIBs (Er et al., 2014; Xie et al., 2014; Lian et al., 2017). Reasonable electrode architecture will be beneficial to the overall performance enhancement of MXene-based anodes.

To address these challenges, researchers have devised a number of strategies, including introduce pores in the surface by chemical etching, increase interlayer spacing by surface modification, and prevent restacking of 2D nanosheets by embedding pillaring materials (Zhao et al., 2015; Ren et al., 2016; Xie et al., 2016; Kajiyama et al., 2017; Luo et al., 2017; Liu et al., 2022). Among these strategies, the melding of MXene and carbon materials has become a highly regarded approach, particularly carbon nanotubes (CNTs) with high conductivity, toughness, and elasticity. For instance, the self-assembled porous MXene/CNTs papers exhibited improved accessibility for electrolytes and showed an excellent sodium-ion storage volumetric performance (Xie et al., 2016). The knotted CNTs are able to simultaneously increase ion accessibility and decrease ion transport route tortuosity (Gao et al., 2020). These advantages make the MXene/CNTs composite a promising material for SIBs and PIBs. However, there is still a need for the development of a straightforward preparation procedure that ensures a strong coupling between MXene and CNTs.

In this study, we developed an *in-situ* approach to achieve superior anodes (MXene@CNTs) for SIBs and PIBs by constructing the three-dimensional (3D) structure of MXene and CNTs. The metal-organic framework (ZIF-67) was chosen as the carbon source for CNTs *in-situ* growth, which was strongly embedded in MXene sheets as pillaring materials to maintain the 3D structure. Additionally, nitrogen-doped CNTs also offer a high way for electron conduction and a buffer layer for volume expansion. In general, this specially designed structure can inhibit restacking of MXene, increase ion accessibility, as well as boost the overall conductivity of the electrodes. When used as anodes in both SIBs and PIBs, MXene@CNTs composites electrodes demonstrated enhanced capacity, rate capability, and cycling stability than MXene electrodes. They could deliver 286 and 250 mAh g^{-1} at 0.05 A g^{-1} for SIBs and PIBs, respectively, and still maintain 208 and 109 mAh g^{-1} at 1 A g^{-1} after cycling.

2 Experimental

2.1 Syntheses of MXene@CNTs

The MXene nanosheets used in this work were prepared by soaking MAX powder in HF for 24 h to remove Al. The composites of MXene and ZIF-67 were then produced using a simple chemical method. Typically, 0.1 g MXene nanosheets and 0.58 g cobalt nitrate were first dispersed in 50 mL methanol to form liquid A. To obtain liquid B, 0.82 g 2-methylimidazole (2MI) was dissolved in 50 mL methanol. While stirring for 30 min, liquid B was added slowly into liquid A. Then, the solution was left undisturbed for 24 h before being filtered to obtain MXene@ZIF-67 powder. Finally, the resultant MXene@ZIF-67 was put into a tube furnace with 2 g of uric acid added upstream. Under Ar atmosphere, the MXene@CNTs were produced by heating to 700 °C for 2 h at a ramping rate of 5 °C min^{-1}.

2.2 Physical characterizations

Scanning electron microscopy (SEM, Hitachi Regulus 8100) and transmission electron microscopy (TEM, FEI Tacnai G2 F20) were utilized to characterize the morphologies and structures. X-ray diffraction (XRD, Bruker D8), Raman spectroscopy (HORIBA LabRAM HR Evolution), and X-ray photoelectron spectroscopy (XPS, Thermo Scientific ESCA LAB 250 Xi) were used to analyze the phases and compositions. Nitrogen adsorption-desorption was conducted to evaluate the surface area and pore distributions (Quantachrome Autosorb).

2.3 Electrochemical measurements

Electrochemical performance analyses of half cells were performed using the 2032-type coin cells. The electrode slurry was made of 80 wt% active material, 10 wt% Super P, and 10 wt % CMC-Na, and then coated on Al foil. After punching, these electrodes were dried overnight at 80 °C. About 1 mg cm^{-2} of active materials was loaded. The assembling process was then carried out within the argon-protected glove box. The counter electrode employed in the experiment was sodium or potassium foil. The separator employed in the experiment was a glass fiber filter (Whatman, Grade GF/A). The electrolyte solution consisted of 1 M $NaClO_4$ EC/DEC with 5% FEC for SIBs and 0.8 M KPF_6 EC/DEC for PIBs.

As for electrochemical performance, the galvanostatic charge-discharge (GCD) process was measured with Neware. The cyclic voltammetry (CV) analysis was performed with electrochemical workstations (Solartron Metrology Ltd Supporting Material 1287 and Supporting Material 1260). The frequency range of the electrochemical impedance spectroscopy (EIS) investigation was 100 kHz to 0.01 Hz. Galvanostatic intermittent titration technique

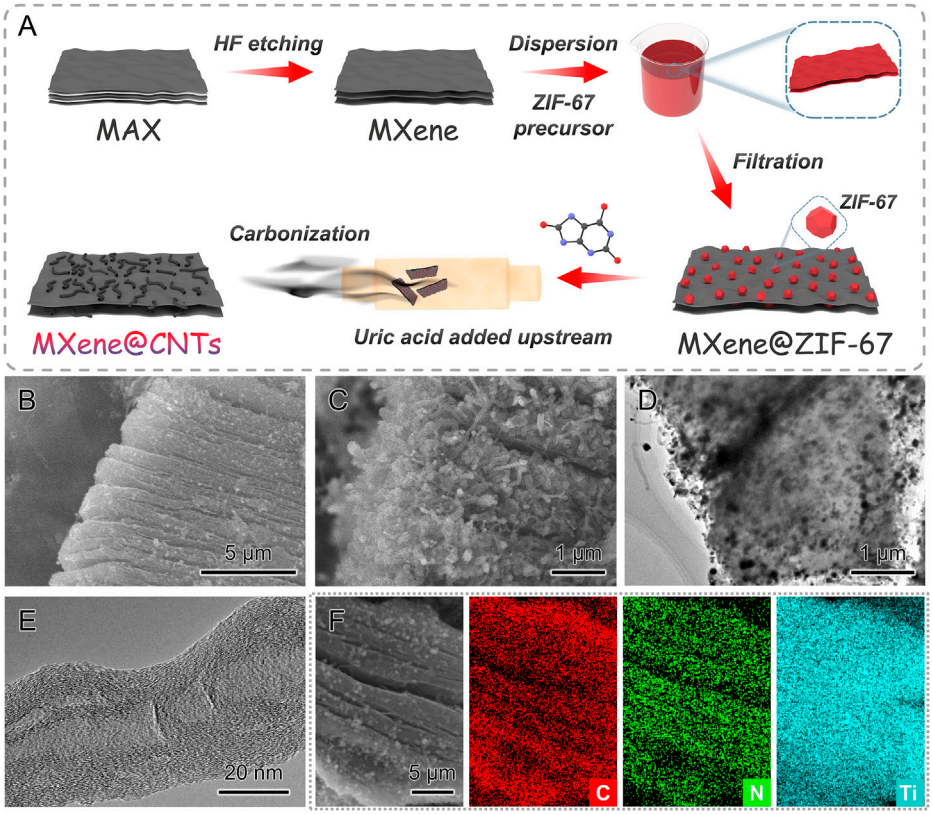

FIGURE 1
Synthetic protocol and morphology of MXene@CNTs. **(A)** Schematic diagram of the fabrication process. **(B, C)** SEM images. **(D, E)** TEM and HRTEM images. **(F)** EDS element mapping.

(GITT) was employed to determine the ion diffusion coefficient in electrodes.

3 Results and discussion

The detailed synthesis procedure of MXene@CNTs is schematically depicted in Figure 1A. Initially, the exfoliated MXene nanosheets were produced by immersing the MAX powder (Ti_3AlC_2) in HF aqueous solution (Supplementary Figures S1 A, B). Second, the cleaned and dried MXene nanosheets were dispersed in a methanol solution to serve as the base for ZIF-67 growth. At the same time, the cobalt precursor and 2MI were successively poured into the above solution. The first added cobalt ions can be deposited on the negatively charged MXene nanosheet through electrostatic interaction, which is convenient for the subsequent reaction with 2MI ligands. The generated ZIF-67 polyhedral particles were affixed to the surface of MXene after aging, and their size was smaller than that it would have been without MXene substrate (Supplementary Figures S1C-F). Finally, considering the close decomposition temperatures, 437 °C for ZIF-67°C and 443 °C for uric acid, we selected the uric acid as the vapor-phase carbon source to catalyze the nitrogen-doped CNTs *in-situ* growth (Kone et al., 2020).

The morphology and microstructure of MXene@CNTs were further analyzed using electron microscopy. As shown in Figure 1B, MXene@CNTs still display a similar delaminated structure as MXene nanosheets, but their surface is covered with velvet-like architecture, forming a unique 3D structure. In the magnified SEM image, the detailed "velvet" can be identified as an aggregate of numerous interconnected nanotubes (Figure 1C). The TEM image also verifies this morphology of nanotubes-coated MXene, and these nanotubes also formed a coating in the interlamellar position of MXene, not just in one part (Figure 1D). According to the high-resolution TEM image (HRTEM), these nanotubes can be determined as carbon nanotubes (CNTs) with approximate 0.35 nm interlayer spacing (Figure 1E). These CNTs show a bamboo-like hollow morphology, which is derived from the catalytic growth of cobalt nanoparticles (Wang et al., 2020). Such a composite structure is capable of providing numerous ion transportation channels, facilitating electrolyte infiltration, and mitigating volume expansion of electrodes. The EDS element mapping reveals an even distribution of C, N, and Ti, which demonstrates the introduction of nitrogen doping by uric acid (Figure 1F).

The successful composite of MXene with ZIF-67 was verified by XRD patterns of MXene@ZIF-67 (Supplementary Figures S2). The crystal structure of MXene@CNTs was further analyzed using XRD. As displayed in Figure 2A, the peaks at 7.1° and 14.5°correspond to

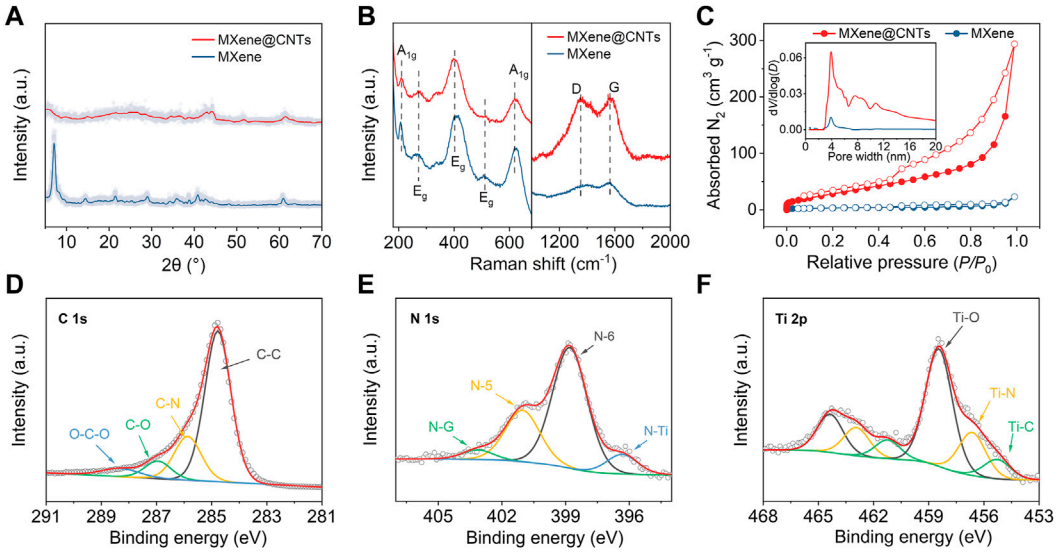

FIGURE 2
Structural and surficial characterization. **(A)** XRD patterns. **(B)** Raman spectra. **(C)** Nitrogen adsorption-desorption isotherms and pore size distributions. High-resolution XPS spectrum of **(D)** C 1s, **(E)** N 1s, **(F)** Ti 2p.

the (002) and (004) reflections of delaminated MXene sheets (Naguib et al., 2012). The (002) peak of MXene@CNTs was located at 6.1°, and the corresponding layer spacing increased from 1.24 nm to 1.45 nm. The weaker (002) peak well confirmed the inhibition of MXene restacking by CNTs. In Raman spectrum of Figure 2B, the MXene@CNTs exhibits the characteristic peaks of MXene and carbon, indicating that they have been successfully composited. Two peaks of 211 and 622 cm^{-1} correspond to the out-of-plane vibrations of Ti and C atoms, while three peaks of 273, 405, and 513 cm^{-1} are in-plane vibrations of Ti, C, and surface functional groups (Yu et al., 2018; Sun et al., 2019). Additionally, the two peaks at 1,361 and 1,572 cm^{-1} contributed to the D-band and G-band of carbon, respectively (Ferrari et al., 2006). Furthermore, the surface area and pore size distribution were analyzed by nitrogen adsorption-desorption isotherms (Figure 2C). The MXene@CNTs shows a type IV adsorption/desorption isotherm with a hysteresis loop, suggesting the coexistence of both mesopores and macropores. The Brunauer–Emmett–Teller (BET) surface area and total pore volume of the MXene@CNTs are 117 $m^2 g^{-1}$ and 0.354 $cm^3 g^{-1}$, respectively. Both are considerably higher than 11 $m^2 g^{-1}$ and 0.019 $cm^3 g^{-1}$ of pure MXene nanosheets. The increased surface area and pore volume further corroborate the significance of CNTs for 3D structure, which is anticipated to increase the ion storage sites and shorten the ion diffusion distance, thereby enhancing rate performance of electrodes.

XPS analysis was performed to elucidate the chemical environment state of MXene@CNTs. The survey XPS spectrum reveals the existence of C, N, O, F, Ti, and Co (Supplementary Figures S3). F is derived from the surface functional groups formed by etching, while Co content of about 1 at% is derived from ZIF-67. As demonstrated in Figure 2D, the C 1s can be deconvoluted into four peaks at 284.8, 285.9, 286.9, and 288.3 eV, corresponding to C-C, C-N, C-O, and O-C-O species, respectively. Notably, the N content in MXenen@CNTs was calculated to be as high as 9.63 at%. The high-resolution N 1s spectrum can be fitted well with four different peaks located at 396.2, 398.8, 401.0, and 403.2 eV, which correspond to the Ti-N, pyridinic (N-6), pyrrolic (N-5), and graphitic N (N-G), respectively (Figure 2E). The small N-Ti peak confirms the nitrogen doping of MXene, which is further confirmed by the Ti-N peak in the Ti 2p spectrum (Figure 2F) (Bao et al., 2018). The nitrogen modification in CNTs and MXene is expected to promote the adsorption of sodium/potassium-ion.

The electrochemical performance of MXene@CNTs in sodium/potassium-ion storage was comprehensively evaluated through a series of electrochemical tests. When applied as anodes for SIBs, MXene@CNTs show a broad reduction peak below 1.0 V on the first CV curve, which can be ascribed to the irreversible chemical reaction between sodium-ion and surface functional groups, along with the development of solid electrolyte interphase (SEI) film (Figure 3A). Then, the near coincidence of the CV curves in the second and third cycles indicates a high reversibility of MXene@CNTs. As shown in Supplementary Figure S4, the sloping GCD profiles indicate the dominating capacitive sodium-ion storage behavior of MXene@CNTs. The initial Coulombic efficiency (ICE) is only 41.1%, resulting from the combination of irreversible reaction and SEI film, which is consistent with the finding of CV analysis. Moreover, a gradual increase in the capacity of subsequent cycles implies the presence of an electrochemical activation process in the MXene@CNTs electrode (Wang et al., 2016). The rate performance of MXene@CNTs and MXene are compared in Figure 3B. MXene@CNTs shows capacities of 286, 246, 223, 188, 157, 124, and 80 mAh g^{-1} at current densities of 0.05, 0.1, 0.2, 0.5, 1.0, 2.0, and 5.0 A g^{-1}, respectively. Significantly greater than 88, 73, 63, 51, 38, 27, and 13 mAh g^{-1} for MXene. The capacity of MXene@CNTs is 6.1 times that of MXene, which further confirms the significance of the modification of CNTs for electron conduction and ion transportation. As for cycling performance, it is worth noting that MXene@CNTs retains 208 mAh g^{-1} after 500 cycles at

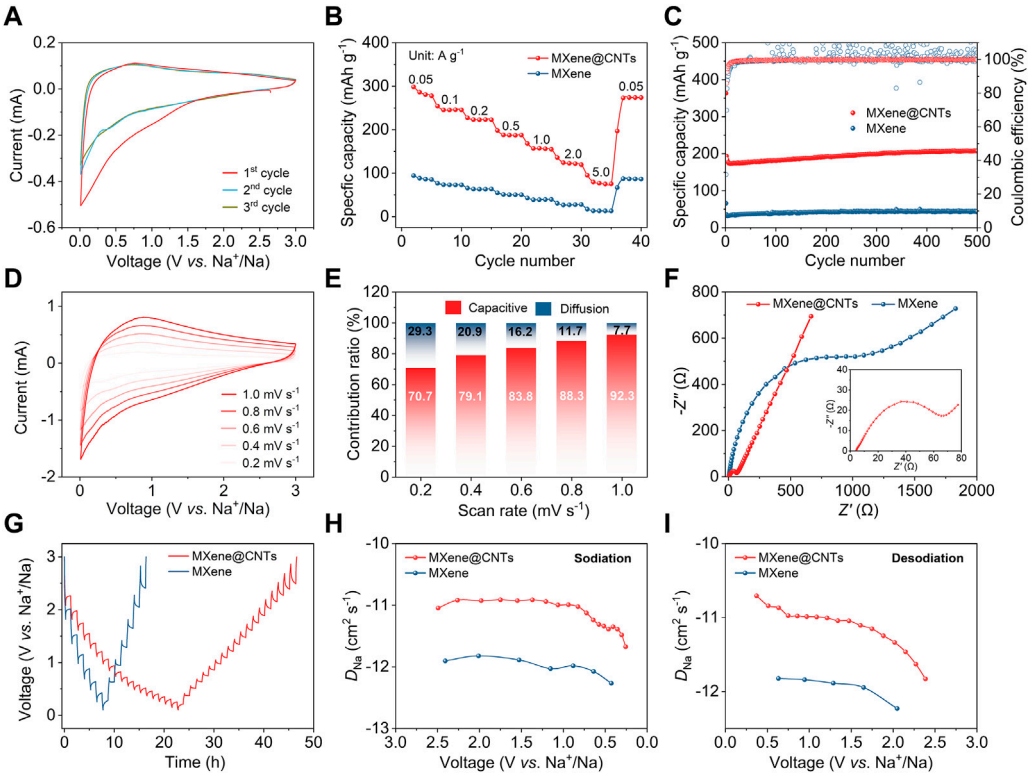

FIGURE 3
Electrochemical performance of SIBs. **(A)** CV curves of MXene@CNTs at 0.2 mV s^{-1}. **(B)** Rate performance. **(C)** Cycling performance at 1.0 A g^{-1}. **(D)** CV curves of MXene@CNTs at scan rates of 0.2–1.0 mV s^{-1}. **(E)** Contribution proportions of capacitive and diffusion at different scan rates. **(F)** EIS patterns. **(G)** GITT profiles. **(H, I)** Chemical diffusion coefficients of sodiation and desodiation processes.

1.0 A g^{-1}, with a capacity retention rate of 107% relative to the second cycle (Figure 3C). This also proves the stability of the composite structure.

To further investigate the kinetics of ion transportation, a half-cell was scanned from 0.2 to 1.0 mV s^{-1} (Figure 3D). The contribution ratios of capacitive effect (k_1v) and diffusion control ($k_2v^{1/2}$) were separated by the Dunn method (Brezesinski et al., 2010). With the increase of scanning rate, the contribution ratio of capacitive effect increases gradually, reaching 92.3% at 1.0 mV s^{-1}. This suggests a capacitive-dominated sodium-ion storage mechanism in MXene@CNTs (Figure 3E). The capacitive contribution of MXene is only 82.4%, indicating the enhancement of active sites by 3D structure and nitrogen doping (Supplementary Figure S5). EIS analysis was further performed to investigate the charge transfer behavior. In the high-frequency region, the semicircle can be attributed to the charge-transfer resistance (R_{ct}), whereas the Warburg impedance is represented by the straight line observed in the low-frequency region. As shown in Figure 3F, the R_{ct} of MXene@CNTs is lower than that of MXene, indicating a quicker charge transfer process. In addition, the Warburg impedance also demonstrates a faster ion transport of sodium-ion in MXene@CNTs.

The GITT was performed to gain a deeper comprehension of the kinetics pertaining to the sodium-ion diffusion coefficient (D_{Na}). Figure 3G shows the voltage response of MXene@CNTs and MXene during the sodiation/desodiation process, and the corresponding diffusion coefficients are calculated. MXene@CNTs exhibits higher D_{Na} than that of MXene, implying faster kinetics performance, which is consistent with the above rate and EIS analysis (Figures 3H,I). All of them show a decreasing D_{Na} during the sodiation process, which may be a repulsive force caused by embedded ions on unembedded ions. Correspondingly, the contribution of repulsive forces during desodiation process also causes the D_{Na} to be higher at the beginning and lower later.

Additionally, the electrochemical performances of MXene@CNTs in PIBs were evaluated. Similar to the above SIBs section, the CV curves also show a broad reduction peak below 1.0 V on the first cycle because of the irreversible reaction and SEI film (Figure 4A). From the second cycle onward, the CV curves show a similar shape, suggesting good reversibility of MXene@CNTs electrode during potassium-ion storage. Accordingly, the first GCD curve reveals an initial Coulombic efficiency of 47.4% (Supplementary Figure S6). The sloping charge/discharge profiles are also consistent well with the CV curves, and all display a capacitive-dominated potassium-ion storage mechanism through adsorption/desorption. As for rate performance, the MXene@CNTs can deliver reversible capacities of 250, 210, 170, 127, 84, 53, and 38 mAh g^{-1} at current densities of 0.05, 0.1, 0.2, 0.5, 1.0, 2.0, and 5.0 A g^{-1}, respectively (Figure 4B). Much higher than 143, 94, 74, 55, 43, 32, and 19 mAh g^{-1} of MXene, demonstrating the significant effect of CNTs on the rate performance. When cycled at 1.0 A g^{-1} for 100 cycles, MXene@CNTs still attain a reversible capacity of

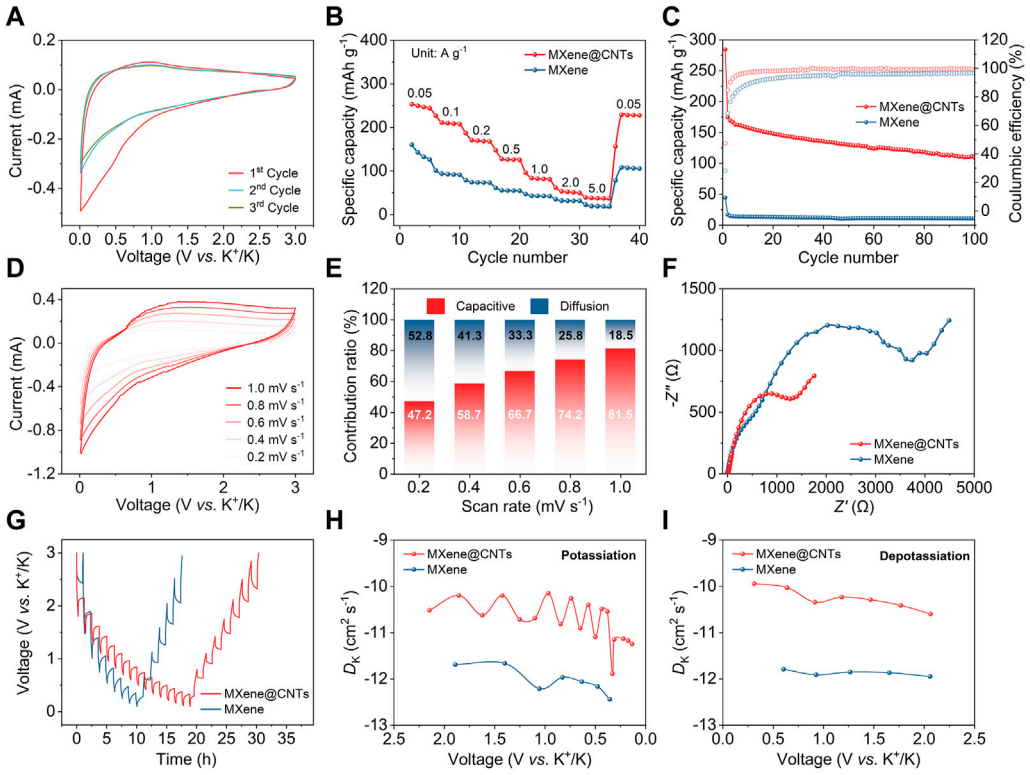

FIGURE 4
Electrochemical performance of PIBs. **(A)** CV curves of MXene@CNTs at 0.2 mV s^{-1}. **(B)** Rate performance. **(C)** Cycling performance at 1.0 A g^{-1}. **(D)** CV curves of MXene@CNTs at scan rates of 0.2–1.0 mV s^{-1}. **(E)** Contribution proportions of capacitive and diffusion at different scan rates. **(F)** EIS patterns. **(G)** GITT profiles. **(H, I)** Chemical diffusion coefficients of potassiation and depotassiation processes.

109 mAh g^{-1} and a Coulombic efficiency of 99.9%, which is better than 11 mAh g^{-1} and 96.6% of MXene, respectively (Figure 4C). Compared to SIBs, the relatively rapid attenuation may be attributable to the destruction of CNTs caused by the intercalation mechanism of large-size potassium-ion, resulting in the deterioration of cycling performance.

In terms of ion transportation kinetics, the contributions of capacitive effect and diffusion control were also studied utilizing CV curves analysis (Figure 4D). As shown in Figure 4E, the capacitive contribution displays an upward trend with the escalation of scan rates, reaching 81.5% at 1.0 mV s^{-1}. It is possible that nitrogen-doped CNTs introduce the intercalation storage mechanism of potassium-ion, resulting in a relatively lower capacitive contribution ratio than that of MXene (Supplementary Figure S7). In EIS spectra, the R_{ct} of MXene@CNTs is smaller than that of MXene, indicating a faster charge transfer process after decorating with CNTs (Figure 4F). The GITT was used to explore the kinetics of potassium-ion storage, and the corresponding diffusivity of potassium-ion (D_K) was evaluated (Figures 4G–I). The D_K of MXene@CNTs is higher than that of MXene in both the potassiation and depotassiation processes. In addition, it could be observed that D_K decreased as the degree of potassiation increased and that it decreased gradually during depotassiation. Just like in the SIBs scenario, this tendency is also due to the repulsive force formed by the pre-embedded potassium-ion, which hinders subsequent ion embedding and pushes ion out.

4 Conclusion

In summary, we have synthesized MXene@CNTs by decorating MXene nanosheets with *in-situ* growth of nitrogen-doped carbon nanotubes. Nitrogen-doped CNTs are utilized to inhibit the stacking of MXene nanosheets to form 3D structures, thereby increasing the active storage sites of ions. This rationally designed anode exhibits significant sodium/potassium-ion storage performance in terms of capacity, rate capability, and cycling stability. The outstanding performance of the MXene@CNTs may be attributed to remarkably improved conductivity through the integration of nitrogen-doped CNTs, which also facilitates electron conduction and ion adsorption. In particular, MXene@CNTs can sustain 80 mAh g^{-1} for SIBs and 38 mAh g^{-1} for PIBs when cycled at 5.0 A g^{-1}, which is 6.1 and 2.0 times that of MXene, respectively. Kinetic analysis reveals that capacitive contribution is primarily responsible for the high-rate capability. These features highlight this MXene@CNTs electrode as an attractive option for advanced energy storage devices, and further promote the practical applications of SIBs and PIBs.

Data availability statement

The raw data supporting the conclusion of this article will be made available by the authors, without undue reservation.

Author contributions

TW, JZ, and XG: Methodology, Formal analysis, Validation, Investigation, Visualization, Writing–original Draft. YM, HY: Investigation, Formal analysis. HZ: Investigation. DD: Investigation. ZS: Investigation. RD: Investigation. YL: Writing–review and editing. JR: Writing–review and editing. XuW: Conceptualization, Validation, Formal analysis, Supervision, Writing–review and editing, Project administration, Funding acquisition. All authors contributed to the article and approved the submitted version.

Funding

The authors acknowledge the support from State Key Laboratory of Catalytic Materials and Reaction Engineering (RIPP, SINOPEC), National Natural Science Foundation of China (52272039, 51972168, 51672124), and High-Performance Computing Center (HPCC) of Nanjing University. The authors declare that this study received funding from State Key Laboratory of Catalytic Materials and Reaction Engineering, Research Institute of Petroleum Processing Co. Ltd (RIPP, SINOPEC). The funder was not involved in the study design, collection, analysis, interpretation of data, the writing of this article or the decision to submit it for publication.

Conflict of interest

Author XG and JR were employed by company Research Institute of Petroleum Processing Co. Ltd. The authors declare that the research was conducted in the absence of any commercial or financial relationships that could be construed as a potential conflict of interest.

Publisher's note

Supplementary material

The supplementary material for this article can be found online at: https://www.frontiersin.org/articles/10.3389/fmats.2023.1214543/full#supplementary-material

References

Armand, M., and Tarascon, J. M. (2008). Building better batteries. *Nature* 451, 652–657. doi:10.1038/451652a

Bao, W. Z., Liu, L., Wang, C. Y., Choi, S., Wang, D., and Wang, G. X. (2018). Facile synthesis of crumpled nitrogen-doped MXene nanosheets as a new sulfur host for lithium-sulfur batteries. *Adv. Energy Mat.* 8, 1702485. doi:10.1002/aenm.201702485

Brezesinski, T., Wang, J., Tolbert, S. H., and Dunn, B. (2010). Ordered mesoporous alpha-MoO_3 with iso-oriented nanocrystalline walls for thin-film pseudocapacitors. *Nat. Mat.* 9, 146–151. doi:10.1038/NMAT2612

Chou, S. L., and Yu, Y. (2017). Next generation batteries: Aim for the future. *Adv. Energy Mat.* 7, 1703223. doi:10.1002/aenm.201703223

Dunn, B., Kamath, H., and Tarascon, J. M. (2011). Electrical energy storage for the grid: A battery of choices. *Science* 334, 928–935. doi:10.1126/science.1212741

Er, D. Q., Li, J. W., Naguib, M., Gogotsi, Y., and Shenoy, V. B. (2014). Ti_3C_2 MXene as a high capacity electrode material for metal (Li, Na, K, Ca) ion batteries. *ACS Appl. Mat. Interfaces* 6, 11173–11179. doi:10.1021/am501144q

Ferrari, A. C., Meyer, J. C., Scardaci, V., Casiraghi, C., Lazzeri, M., Mauri, F., et al. (2006). Raman spectrum of graphene and graphene layers. *Phys. Rev. Lett.* 97, 187401. doi:10.1103/PhysRevLett.97.187401

Gao, X., Du, X., Mathis, T. S., Zhang, M. M., Wang, X. H., Shui, J. L., et al. (2020). Maximizing ion accessibility in MXene-knotted carbon nanotube composite electrodes for high-rate electrochemical energy storage. *Nat. Commun.* 11, 6160. doi:10.1038/s41467-020-19992-3

Ghidiu, M., Lukatskaya, M. R., Zhao, M. Q., Gogotsi, Y., and Barsoum, M. W. (2014). Conductive two-dimensional titanium carbide 'clay' with high volumetric capacitance. *Nature* 516, 78–81. doi:10.1038/nature13970

Hosaka, T., Kubota, K., Hameed, A. S., and Komaba, S. (2020). Research development on K-ion batteries. *Chem. Rev.* 120, 6358–6466. doi:10.1021/acs.chemrev.9b00463

Huang, W. H., Su, C. Y., Zhu, C., Bo, T. T., Zuo, S. W., Zhou, W., et al. (2023). Isolated electron trap-induced charge accumulation for efficient photocatalytic hydrogen production. *Angew. Chem. Int. Ed.*, e202304634. doi:10.1002/ange.202304634

IEA (2022). *World energy outlook 2022*. https://www.iea.org/reports/world-energy-outlook-2022 (Accessed April 15, 2023).

Kajiyama, S., Szabova, L., Iinuma, H., Sugahara, A., Gotoh, K., Sodeyama, K., et al. (2017). Enhanced Li-ion accessibility in MXene titanium carbide by steric chloride termination. *Adv. Energy Mat.* 7, 1601873. doi:10.1002/aenm.201601873

Kone, I., Ahmad, Z., Xie, A. O., Tang, Y., Sun, Y. Z., Chen, Y. M., et al. (2020). *In situ* growth of Co_4N nanoparticles-embedded nitrogen-doped carbon nanotubes on metal-organic framework-derived carbon composite as highly efficient electrocatalyst for oxygen reduction and evolution reactions. *Energy Technol.* 8, 2000409. doi:10.1002/ente.202000409

Li, C. P., Qiu, M., Li, R. L., Li, X., Wang, M. X., He, J. B., et al. (2022). Electrospinning engineering enables high-performance sodium-ion batteries. *Adv. Fiber Mat.* 4, 43–65. doi:10.1007/s42765-021-00088-6

Lian, P. C., Dong, Y. F., Wu, Z. S., Zheng, S. H., Wang, X. H., Wang, S., et al. (2017). Alkalized Ti_3C_2 MXene nanoribbons with expanded interlayer spacing for high-capacity sodium and potassium ion batteries. *Nano Energy* 40, 1–8. doi:10.1016/j.nanoen.2017.08.002

Liang, X., Garsuch, A., and Nazar, L. F. (2015). Sulfur cathodes based on conductive MXene nanosheets for high-performance lithium-sulfur batteries. *Angew. Chem. Int. Ed.* 127, 3907–3911. doi:10.1002/anie.201410174

Lin, M. C., Gong, M., Lu, B. G., Wu, Y. P., Wang, D. Y., Guan, M. Y., et al. (2015). An ultrafast rechargeable aluminium-ion battery. *Nature* 520, 324–328. doi:10.1038/nature14340

Liu, Y. P., Wang, D., Zhang, C., Zhao, Y., Ma, P. M., Dong, W. F., et al. (2022). Compressible and lightweight MXene/carbon nanofiber aerogel with "layer-strut" bracing microscopic architecture for efficient energy storage. *Adv. Fiber Mat.* 4, 820–831. doi:10.1007/s42765-022-00140-z

Lukatskaya, M. R., Mashtalir, O., Ren, C. E., Dall'Agnese, Y., Rozier, P., Taberna, P. L., et al. (2013). Cation intercalation and high volumetric capacitance of two-dimensional titanium carbide. *Science* 341, 1502–1505. doi:10.1126/science.1241488

Luo, J. M., Zhang, W. K., Yuan, H. D., Jin, C. B., Zhang, L. Y., Huang, H., et al. (2017). Pillared structure design of MXene with ultralarge interlayer spacing for high-performance lithium-ion capacitors. *ACS Nano* 11, 2459–2469. doi:10.1021/acsnano.6b07668

Luo, X., Wang, J. H., Dooner, M., and Clarke, J. (2015). Overview of current development in electrical energy storage technologies and the application potential in power system operation. *Appl. Energy* 137, 511–536. doi:10.1016/j.apenergy.2014.09.081

Naguib, M., Mashtalir, O., Carle, J., Presser, V., Lu, L., Hultman, L., et al. (2012). Two-dimensional transition metal carbides. *ACS Nano* 6, 1322–1331. doi:10.1021/nn204153h

Naguib, M., Mochalin, V. N., Barsoum, M. W., and Gogotsi, Y. (2014). 25th anniversary article: MXenes: A new family of two-dimensional materials. *Adv. Mat.* 26, 992–1005. doi:10.1002/adma.201304138

Ren, C. E., Zhao, M. Q., Makaryan, T., Halim, J., Boota, M., Kota, S., et al. (2016). Porous two-dimensional transition metal carbide (MXene) flakes for high-performance Li-ion storage. *ChemElectroChem* 3, 689–693. doi:10.1002/celc.201600059

Shi, F. Y., Chen, C. H., and Xu, Z. L. (2021). Recent advances on electrospun nanofiber materials for post-lithium ion batteries. *Adv. Fiber Mat.* 3, 275–301. doi:10.1007/s42765-021-00070-2

Sun, J., Lee, H. W., Pasta, M., Yuan, H. T., Zheng, G. Y., Sun, Y. M., et al. (2015). A phosphorene-graphene hybrid material as a high-capacity anode for sodium-ion batteries. *Nat. Nanotechnol.* 10, 980–985. doi:10.1038/NNANO.2015.194

Sun, N., Zhu, Q., Anasori, B., Zhang, P., Liu, H., Gogotsi, Y., et al. (2019). MXene-bonded flexible hard carbon film as anode for stable Na/K-ion storage. *Adv. Funct. Mat.* 29, 1906282. doi:10.1002/adfm.201906282

Tian, Y. S., Zeng, G. B., Rutt, A., Shi, T., Kim, H., Wang, J. Y., et al. (2021). Promises and challenges of next-generation "beyond Li-ion" batteries for electric vehicles and grid decarbonization. *Chem. Rev.* 121, 1623–1669. doi:10.1021/acs.chemrev.0c00767

Wang, C. H., Kim, J., Tang, J., Kim, M., Lim, H., Malgras, V., et al. (2020). New strategies for novel MOF-derived carbon materials based on nanoarchitectures. *Chem* 6, 19–40. doi:10.1016/j.chempr.2019.09.005

Wang, N. N., Chu, C. X., Xu, X., Du, Y., Yang, J., Bai, Z. C., et al. (2018). Comprehensive new insights and perspectives into Ti-based anodes for next-generation alkaline metal (Na^+, K^+) ion batteries. *Adv. Energy Mat.* 8, 1801888. doi:10.1002/aenm.201801888

Wang, S. Q., Xia, L., Yu, L., Zhang, L., Wang, H. H., and Lou, X. W. (2016). Free-standing nitrogen-doped carbon nanofiber films: Integrated electrodes for sodium-ion batteries with ultralong cycle life and superior rate capability. *Adv. Energy Mat.* 6, 1502217. doi:10.1002/aenm.201502217

Wu, X., Zhang, H. B., Zuo, S. W., Dong, J. C., Li, Y., Zhang, J., et al. (2021). Engineering the coordination sphere of isolated active sites to explore the intrinsic activity in single-atom catalysts. *Nano-Micro Lett.* 13, 136. doi:10.1007/s40820-021-00668-6

Xie, X., Zhao, M. Q., Anasori, B., Maleski, K., Ren, C. E., Li, J. W., et al. (2016). Porous heterostructured MXene/carbon nanotube composite paper with high volumetric capacity for sodium-based energy storage devices. *Nano Energy* 26, 513–523. doi:10.1016/j.nanoen.2016.06.005

Xie, Y., Dall'Agnese, Y., Naguib, M., Gogosti, Y., Barsoum, M. W., Zhuang, H. L. L., et al. (2014). Prediction and characterization of MXene nanosheet anodes for non-lithium-ion batteries. *ACS Nano* 8, 9606–9615. doi:10.1021/nn503921j

Yabuuchi, N., Kubota, K., Dahbi, M., and Komaba, S. (2014). Research development on sodium-ion batteries. *Chem. Rev.* 114, 11636–11682. doi:10.1021/cr500192f

Yang, E., Ji, H., Kim, J., Kim, H., and Jung, Y. (2015). Exploring the possibilities of two-dimensional transition metal carbides as anode materials for sodium batteries. *Phys. Chem. Chem. Phys.* 17, 5000–5005. doi:10.1039/c4cp05140h

Yu, L. Y., Hu, L. F., Anasori, B., Liu, Y. T., Zhu, Q. Z., Zhang, P., et al. (2018). MXene-bonded activated carbon as a flexible electrode for high-performance supercapacitors. *ACS Energy Lett.* 3, 1597–1603. doi:10.1021/acsenergylett.8b00718

Zhang, H. B., Zuo, S. W., Qiu, M., Wang, S. B., Zhang, Y. F., Zhang, J., et al. (2020). Direct probing of atomically dispersed Ru species over multi-edged TiO_2 for highly efficient photocatalytic hydrogen evolution. *Sci. Adv.* 6, eabb9823. doi:10.1126/sciadv.abb9823

Zhao, M. Q., Ren, C. E., Ling, Z., Lukatskaya, M. R., Zhang, C. F., Van Aken, K. L., et al. (2015). Flexible MXene/carbon nanotube composite paper with high volumetric capacitance. *Adv. Mat.* 27, 339–345. doi:10.1002/adma.201404140

Zhu, Z. X., Jiang, T. L., Ali, M., Meng, Y. H., Jin, Y., Cui, Y., et al. (2022). Rechargeable batteries for grid scale energy storage. *Chem. Rev.* 122, 16610–16751. doi:10.1021/acs.chemrev.2c00289